Original Paper

Landslides
DOI 10.1007/s10346-025-02579-8
Received: 10 March 2025
Accepted: 1 July 2025

José Juan de Sanjosé-Blasco · Mariló López · Enrique Serrano · Estrella Alonso · Javier Rodrigo

Evolution of debris cones with TLS (2009–2024) and development of predictive techniques with functional data

Abstract This study aims to analyse the dynamic of two debris cones (Cone A and Cone B) in Picos de Europa in the northern Iberian Peninsula. Terrestrial laser scanning (TLS) technology was used for their continuous assessment every August for 16 years (2009–2024). The statistical predictive value of position (*Z*) in 2024 was calculated for the same planimetric position (*X*, *Y*) throughout all the profiles of maximum slopes of the digital elevation model (DEM) of 2009. To do so, we interpolated the actual field data from 2009 to 2023 and used them to form a sample of curves, which are interpreted as the realization of a functional random variable that can be predicted using statistical techniques. The predictive curve obtained was compared with the 2024 field data. The results of both coordinates (*Z*), the actual field data, and the statistical data are coherent within the margin of error of the data collection. The observations and calculations of the two debris cones were treated independently, but both showed the same behaviour. In this way, the present study demonstrates the goodness of some statistical techniques for the functional analysis of data that allow predicting displacement curves by adjusting the model to the sample of movement curves from previous years.

Keywords Picos de Europa · Debris cones · Terrestrial laser scanning · Mathematical modelling

Introduction

In temperate highlands, among the quickest mechanisms of sediment transference are taluses and debris cones, which are highly prevalent slope formations. The materials originate from walls due to weathering and channels, and the processes involved vary greatly. While rockfalls, snow avalanches and debris flows are the primary processes in the debris dynamic, surface processes such as creep, rolling, solifluction, physical and chemical weathering, and surface runoff are also present (Kotarba et al. 1979; Selby 1982; Gardner 1983; Luckman 1988). The dynamics of debris cones and active taluses are currently interpreted in the context of paraglacial settings that support rockfalls, mass displacements, and debris talus changes (Ballantyne 2002).

Channels and walls are the sources of debris, creating a cascading sedimentary system (Schrott and Adams 2002; Otto et al. 2009). The processes involved are nivation, debris flows, solifluction, or gelifluction, plant colonization, trampling by animals, and anthropogenic intervention, such as paths and infrastructure, which all contribute alterations with high spatial and temporal variability (Becht et al. 2005; Reynard et al. 2012). The potential of remote methods, such as terrestrial laser scanning (TLS) and photogrammetry with unmanned aerial vehicles (UAV), is widely recognized for the study of debris flow, debris talus, and cone volumes in numerous temperate mountains (Sass and Krautblatter 2007; Papa et al. 2016; Serrano et al. 2019).

The post-depositional processes, which configure the stratified structure through nivation and debris flows, were identified using theoretical models (Hétu and Vandelac 1989; Hétu 1990). Mathematical formulation has been used to analyse the dynamic relationships among walls, taluses, and processes (Carson 1977; Bithell et al. 2014). A discrete element model that searches the dynamic of each particle after its fall has been created based on the evolution of the slope of the taluses (Bithell et al. 2014).

The aim of this paper is to study and predict the temporal evolution of the behaviour of debris cones, broadening knowledge of spatial and temporal changes. The techniques introduced in recent years for the prediction and analysis of functional data are considered to be suitable. These techniques respect the continuous nature of the phenomenon, unlike the statistical techniques applied to multivariant data, in which the data sample that was previously made up of vectors (de Sanjosé-Blasco et al. 2020) now consists of curves (Bosq 2000; Ramsay and Silverman 2005; Mas and Pumo 2009).

Study area

The central massif of the Picos de Europa (Fig. 1) reaches an altitude of 2648 m above sea level (m a.s.l.), and the proximity of the sea gives it an oceanic climate defined by intense snowfall and precipitation, which surpasses 2500 mm·a^{-1} at the summits. The relief of the Picos de Europa is characterized by its geological structure, karst, and glacial morphogenic systems. The high mountain environment is today dominated by nival and periglacial processes. The investigation of periglacial processes in the Picos de Europa has focused on the distribution of active landforms and processes, including patterned grounds, ice mounds, solifluction lobes, ploughing blocks or ice patches (González-Trueba 2007), taluses, and debris cones (González-Trueba and Serrano 2010; Serrano and González-Trueba 2010; Serrano et al. 2011), as well as the potential presence of mountain permafrost (Pisabarro et al. 2017).

The Peña Vieja Group (2614 m a.s.l.) is in the central massif and is made up of overlying thrusts to the south divided by fractures (Farias 1982) that generate a succession of dorsal ramps with a dip of the materials towards the north. The thrust's front produces abrupt south-pointing scarps. From Peña Vieja (2614 m a.s.l.) to the peak Tesorero (2570 m a.s.l.) (Fig. 1), the entire set rises more

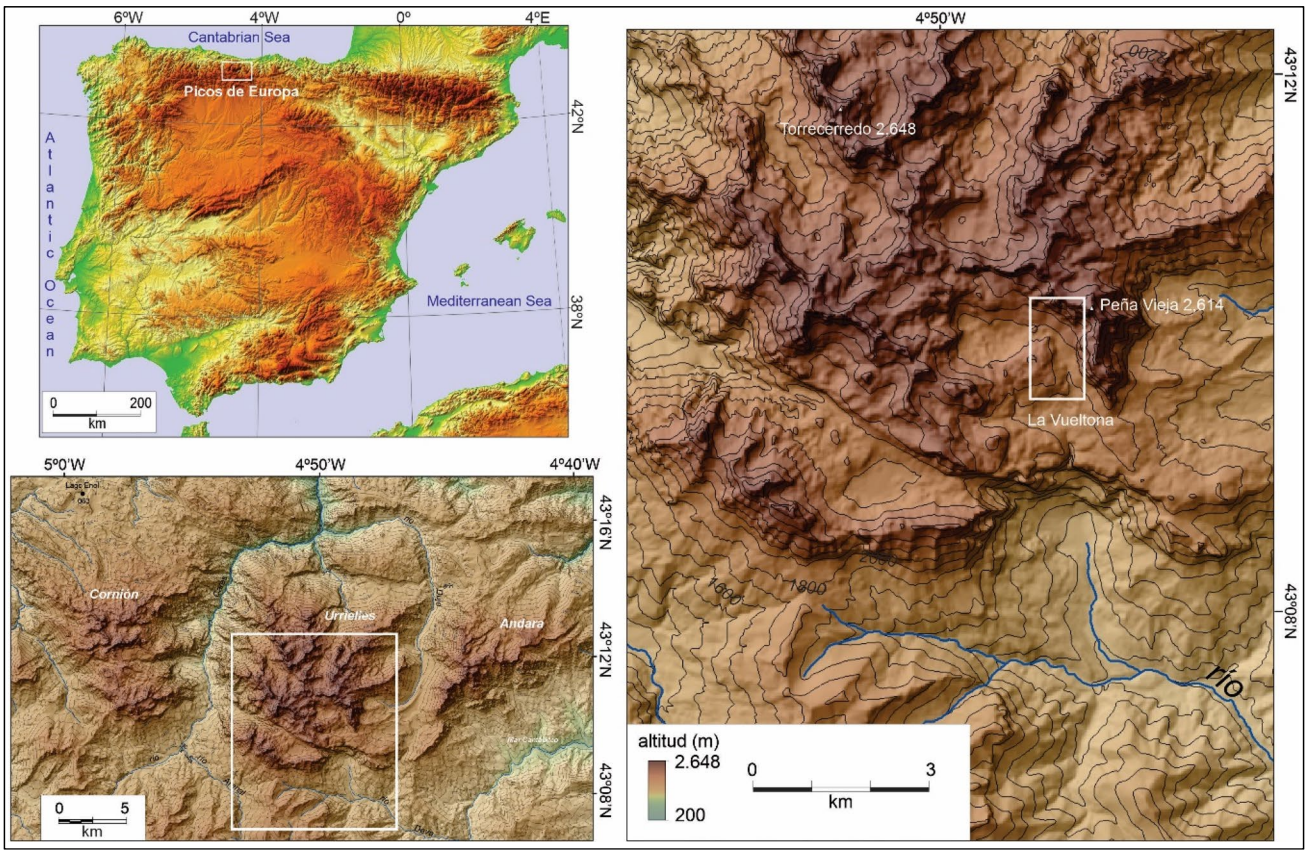

Fig. 1 Location of the study area and debris cones: **A** Cantabrian Mountains in the north of Iberian Peninsula. **B** Location of the Picos de Europa massifs. **C** The Central Massif of Picos de Europa and location of debris cones on the south face of Peña Vieja

than 400 m above the surrounding materials, creating a continuous scarp to 2300 m a.s.l.

The annual air medium temperature (AAMT) around the debris cones is of 3.6 °C at Verónica Hutte (2325 m a.s.l. and 1700 m far from the debris cone), and 6 °C at the Cable Car (1823 m a.s.l. and 1800 m far from the debris cone). Annual medium precipitation is around 608.05 mm a^{-1} (2009–2014 at 1800 m a.s.l.) and 2636 mm a^{-1} (2008–2015 at 2325 m a.s.l.), typical of a high mountain Atlantic climate. The thermal regime shows a large difference between the ground and the air (Pisabarro et al. 2017; Serrano et al. 2019) with an AAMT around 2.4 °C higher in the lower part of the cones than in the upper areas. The snow cover is very important for the ground thermal regime, and only in the years with a thin or short-lasting snow cover did ground temperatures reach − 1 °C/− 2 °C (Pisabarro et al. 2017). The duration of the snow cover is highly variable, between two and seven months. The high variability of the snow cover and the moderate temperatures implies the existence of melt processes and water flow on the snow surface during the winter and spring periods. Slab avalanches lead to snow over-accumulation and a late melt in the lower parts of the debris cones. The implications for the water availability and ground thermal regime are very important. The freeze and frost shattering affects the walls, which remained free of snow in all years, whereas on the debris cones, this was minimal due to the low altitude and snow protection. Thus, cryogenic processes have a very modest presence in the analysed debris cones.

A wide representation of landforms includes inherited and active ones. Inactive landforms that have formed in a paraglacial climate over the past 12,000 years include layered debris, solifluction lobes, and rock glaciers (Serrano and González-Trueba 2004; González-Trueba 2007; Serrano et al. 2012). Debris taluses and debris cones are active and semi-active landforms located between 1200 m a.s.l. and 2600 m a.s.l. and are all active above 2000 m a.s.l. (González-Trueba 2007; Serrano and González-Trueba 2004; Serrano et al. 2019). The material brought on the slopes came from the walls, where the weathering related to periglacial and thermal processes as well as the tectonic weaknesses generate rockfalls towards the narrow and steep channels where debris are transported towards the cone.

On the debris cone surfaces, there are four dominant surface processes. The main ones are metric to decametric debris lobes and block streams. Debris flow, characterized by depth channels of between 1 and 3 m, is the faster and more efficient debris transfer systems moving sediments from the proximal to the distal parts. The proximal part is characterized by small debris flow channels and scattered boulders with finer debris (Serrano et al. 2019). Debris flow activity has been detected twice during the last 14 years (2011 and 2013).

Two important processes of redistribution of materials on the surface of the cones are slide and creep. Rockfalls also generate boulders scattered throughout the cones by rolling and creeping, although the sliding fabric indicates both sliding over a seasonal snow cover and creeping. The boulders are mainly falling and rolling boulders that have come to rest at the edge of the cones, but sliding fabric is also common. The central part is dominated by metric sized debris lobes with scattered boulders and depth debris flow channels sometimes depositing debris fan. The distal part is the most complex. The debris fans boulders and finer debris are scattered with sliding fabric and flow movement.

Methodology

Data collection by TLS

In the area of La Vueltona (Picos de Europa), two debris cones were chosen to associate with the morpho structural conditions that were favoured by the presence of a wall of over 400 m with the unstable materials and with morphoclimatic conditions driving the gravitational, cryogenic, or nival processes to different altitudes (Fig. 2).

The terrestrial laser scanning (TLS) geomatic approach was followed continuously every August for 16 years (2009–2024) in order to analyse the debris cones' surface alterations and dynamic changes. The tool used was the 'Image Station' (Topcon) total station, which can scan over 1000 m with a positional inaccuracy of 2 cm from the point measured. A 3 × 3-m measuring grid was created from the scanning base for the two debris cones, and a 40 × 40-cm grid was created for the debris flow channel that grooved the left side of cone B. Although the computations were handled separately, the origin was the same for both cones despite using a local coordinate system.

The digital elevation model (DEM), which is based on a triangulated irregular network (TIN) and permits for the calculation of annual spatial fluctuations in volume, was created from the grid of points. Furthermore, six maximum slope profiles were created (in 2009) for each debris cone to understand their dynamic behaviour. The rock material that fell from the walls surrounding the debris cones follows the path of a maximum slope line, which is why these profiles were selected.

The cone material was no larger than 30 cm, except cone B, which had blocked in the distal portion of over a meter in size.

Mathematical modelling

The values of the profiles for 2024 were predicted using data gathered from the debris cones every year from 2009 to 2023 (Table 1). It was taken into consideration for these computations that, even though the data from prior years are made up of a discrete set of numbers, they actually belong to the annual curves that show how a continuous process evolves. The methods developed in recent years are considered appropriate for the analysis and prediction of functional data due to the nature of the phenomenon (Bosq 2000; Ramsay 2005; Mas and Pumo 2009). These techniques respect the continuous nature of the phenomenon as opposed to the statistical techniques applied to multivariate data.

The difference between functional data prediction and statistical techniques applied to multivariate data lies primarily in the nature of the data being analyzed and how they are represented:

- In the case of multivariate data, these are observations represented as vectors of variables. Each observation is a point in a finite space (R^n).
- In the case of functional data, observations are functions, curves, or continuous trajectories. Statistical tools must be adapted to handle functions, not vectors.

For the predictive analysis performed in this article, an autoregressive model of the first order, developed by Bosq (2000), was applied as provided by the following equation:

$$X_{n+1} = \Psi(X_n) + \varepsilon_{n+1} \quad (1)$$

where the error ε_n and observations X_n are curves, and Ψ is a linear operator that transforms one curve into another. An estimator $\widehat{\Psi}$ of operator Ψ will be obtained, fitted by applying the historical series of the functional sample $\{X_1, X_2, \ldots, X_n\}$, and will provide the prediction of X_{n+1} as $\widehat{X}_{n+1} = \widehat{\Psi}(X_n)$.

The functional operator Ψ acting on a curve X is considered to be an integral operator:

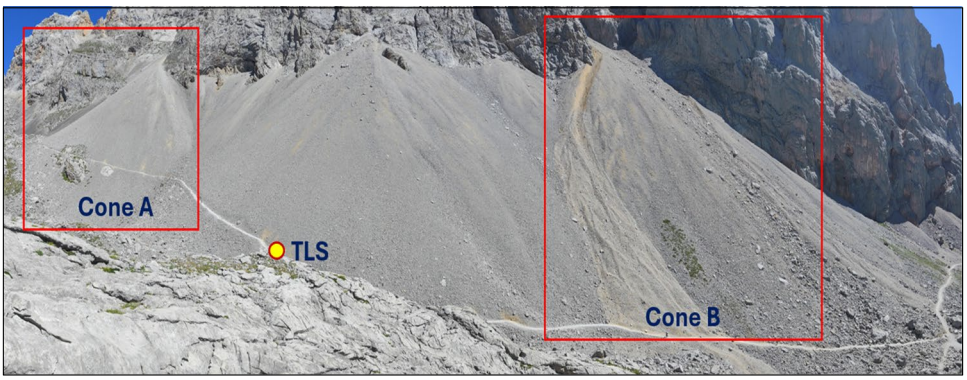

Fig. 2 Photograph of Cone A and Cone B including terrestrial laser scanning (TLS) station. The source area of debris cone material is the weathered and tectonically weakened limestone walls

Table 1 Dynamic between points 21 and 30 of profile 4 of cone A for the period 2009–2024

	2009	2010	2011	2012	2013	2014	2015	2016	2017	2018	2019	2020	2021	2022	2023	2024
21	2624.125	2624.504	2624.481	2624.389	2624.273	2624.366	2624.162	2623.844	2623.796	2624.390	2624.367	2624.213	2624.399	2624.478	2624.269	2603.125
22	2623.406	2623.791	2623.738	2623.668	2623.572	2623.647	2623.442	2623.175	2623.135	2623.670	2623.655	2623.506	2623.702	2623.760	2623.545	2601.406
23	2622.687	2623.077	2623.017	2622.947	2622.866	2622.928	2622.723	2622.507	2622.474	2622.949	2622.943	2622.800	2622.987	2623.042	2622.821	2599.687
24	2621.967	2622.355	2622.296	2622.226	2622.160	2622.208	2622.005	2621.840	2621.813	2622.228	2622.231	2622.100	2622.272	2622.323	2622.097	2597.967
25	2621.248	2621.629	2621.574	2621.504	2621.455	2621.487	2621.363	2621.175	2621.153	2621.507	2621.518	2621.407	2621.557	2621.603	2621.372	2596.248
26	2620.543	2620.905	2620.850	2620.782	2620.751	2620.766	2620.688	2620.513	2620.494	2620.786	2620.806	2620.714	2620.841	2620.882	2620.649	2594.543
27	2619.852	2620.181	2620.127	2620.059	2620.048	2620.045	2619.982	2619.853	2619.835	2620.064	2620.094	2620.021	2620.125	2620.161	2619.926	2592.852
28	2619.161	2619.458	2619.413	2619.337	2619.346	2619.324	2619.276	2619.195	2619.177	2619.349	2619.381	2619.328	2619.409	2619.440	2619.241	2591.161
29	2618.471	2618.735	2618.703	2618.627	2618.645	2618.603	2618.590	2618.538	2618.520	2618.639	2618.670	2618.635	2618.694	2618.718	2618.554	2589.471
30	2617.780	2618.013	2617.993	2617.920	2617.957	2617.882	2617.905	2617.881	2617.863	2617.929	2617.958	2617.941	2617.978	2617.997	2617.852	2587.780

$$\Psi(X)(t) = \int_0^1 \psi(t,s)X(s)ds \tag{2}$$

in which $\psi(t,s)$ is the kernel of the operator Ψ, being s the integration variable.

The predictive methods in the literature differ in their choice of the operator kernel estimate $\widehat{\psi}(t,s)$. After several initial comparisons using different kernel estimators, the EK developed in Section 2 of Didericksen et al. (2011) was chosen, which gives very good results.

In Sanjosé-Blasco et al. (2020), following several initial comparisons using different estimators of the kernel, the estimated kernel (EK) was chosen, developed in Section 2 of Didericksen et al. (2011), as it was the one that provided the best sample of estimates of those applying classical methods. In Section 4 of this article, an improved estimate is developed as an alternative to estimate the kernel, called the estimated kernel improved (EKI), which as has already been confirmed, makes worse estimates than EK in the specific case of our study.

For these reasons, the present study compares the prediction obtained using the estimate of the kernel used (EK) in Sanjosé-Blasco et al. (2020) with a variant of EKI (called VEKI), which was developed by the authors of this article, which provides better predictive results than EK or EKI.

As described by Didericksen et al. (2011), in EK, the use of estimates of autovalues of the main functional components of observations X_n is proposed, ordered from larger to smaller $\{a, b, c\}$. In the estimate, EKI was proposed to substitute $\{a, b, c\}$ for $\{a, b, c + 1.5(a + b)\}$.

The novelty put forward by the authors of this article is to use a variant of EKI, called VEKI, in which in most cases (in 17 of the 18 errors calculated), better results are obtained than when using EKI, used in Sanjosé-Blasco et al. (2020). The variant VEKI consists of substituting the estimates of the autovalues $\{a, b, c\}$ for $\{a, b+1.5(a+\mathrm{b}), c+1.5(a+\mathrm{b})\}$ and later re-ordering these values from greater to smaller.

Results

In order to obtain the estimates of the kernel $\psi(t,s)$, which determine the methods previously mentioned, some changes must be made in the original available sample.

In this particular problem, the initial data sample measured in metres comprises discrete values obtained annually from 2009 to 2023. The values corresponding to each of these years are uniformly distributed within the interval [0,1] and are interpolated by splines to form 15 curves that give rise to up the functional sample $\{C_1, \ldots, C_{15}\}$.

Work is performed on the differences in the curves of two consecutive years and with a centred sample. In order to do so, the mean functional sample is subtracted from the difference between two consecutive curves.

In this way, once the initial sample has been dealt with, work begins with a functional sample of 14 curves $\{X_1, \ldots, X_{14}\}$ with $X_i = (C_{i+1} - C_i) - \frac{1}{14}\sum_{j=1}^{14}(C_{j+1} - C_j)$, and $i = 1, \ldots, 14$. The curves are defined within the interval [0,1] and return values in metres.

Once the estimator of the kernel of the operator is done $\widehat{\psi}(t,s)$, calculated following the steps described in the aforementioned study (Didericksen et al. (2011) but using the modification of that

of the variant VEKI mentioned earlier, we obtain the estimate of operator $\widehat{\Psi}(X)$. Therefore, the prediction X_{15} can be obtained as given by $\widehat{X}_{15} = \widehat{\Psi}(X_{14})$.

This methodology may be applied to any of the profiles from which data have been collected (Fig. 3). In our case, once the data have been used as described in the previous paragraph, work begins with six samples from 14 curves, $\{X_1, \ldots, X_{14}\}$, in which each sample corresponds to each of the six profiles denoted for cone A: A2, A3, A4, and for cone B: B3, B4, B5 (in order of appearance in Fig. 3).

As previously mentioned, the prediction $\widehat{X}_{15}$ selected was obtained using the method VEKI (a variant of the classical method of EKI) in each of the six profiles, and shown in red, together with the sample in Fig. 4.

If a $\widehat{X}_{15}$ is added to the functional mean $\frac{1}{14}\sum_{j=1}^{14}(C_{j+1} - C_j)$, it provides the prediction of the difference between 2024 and 2023, and therefore, adding in the data from 2023, the prediction of the curve in 2024 can be obtained, as denoted by C_{16}, and we can thus estimate the discrete values of 2024.

Parallel with these calculations, the field data for 2024 were obtained. Figure 5 shows the difference between the graph of interpolated data from the prediction obtained using the method VEKI for the year 2024 and the graph of the real interpolated data of 2024 in each of the six profiles.

Discussion

The prediction for 2024, by means of mathematical procedures using the annual data from the period 2009–2023 and the field measurement of 2024, reveals the difference between the predictive curve and that measured.

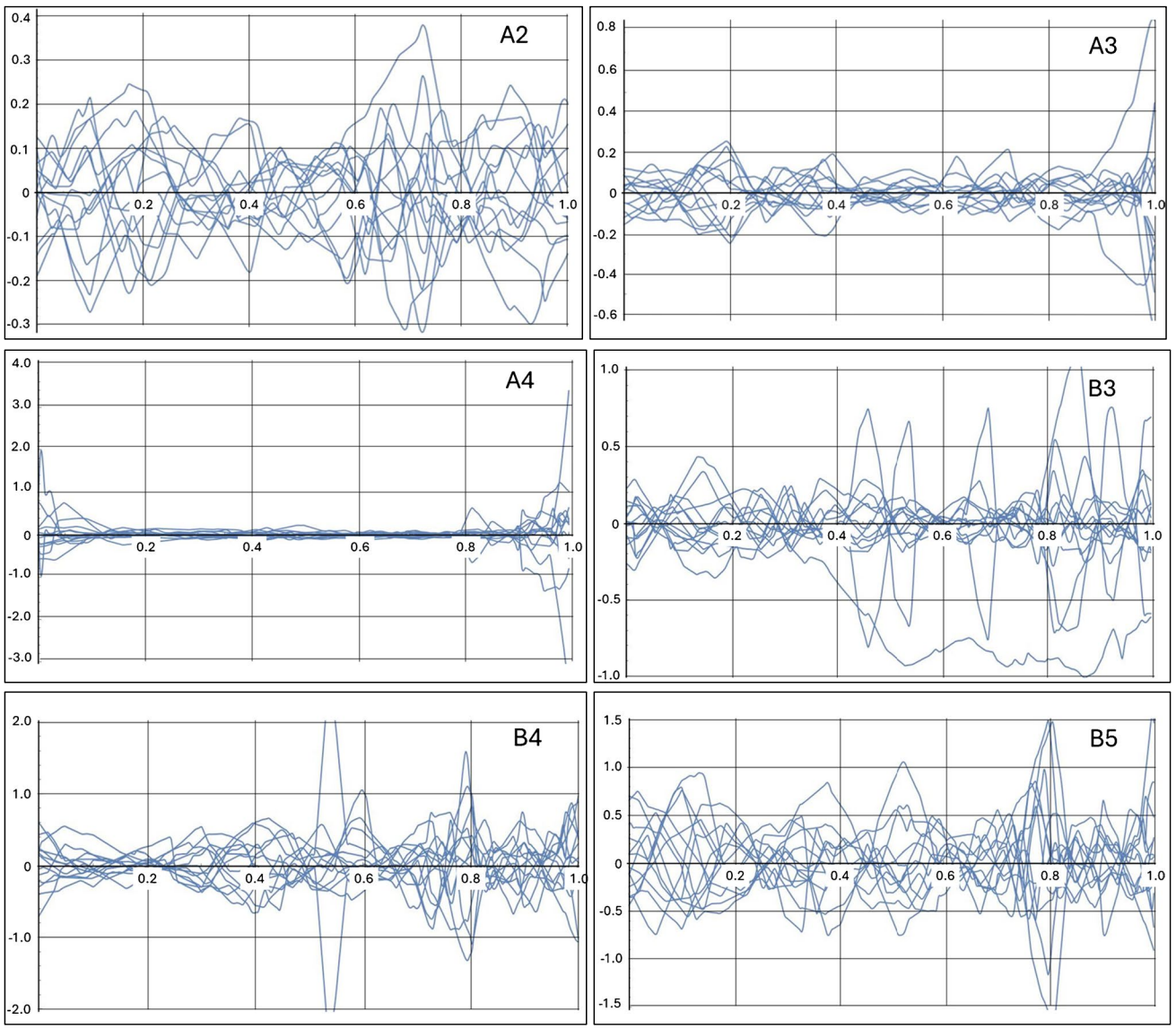

Fig. 3 Sample obtained for the six profiles: Cone A (A2, A3, A4) and Cone B (B3, B4, B5), in which each graph shows the 14 curves of each of the six profiles, processed from the data, defined in the interval [0,1] and returning values in metres

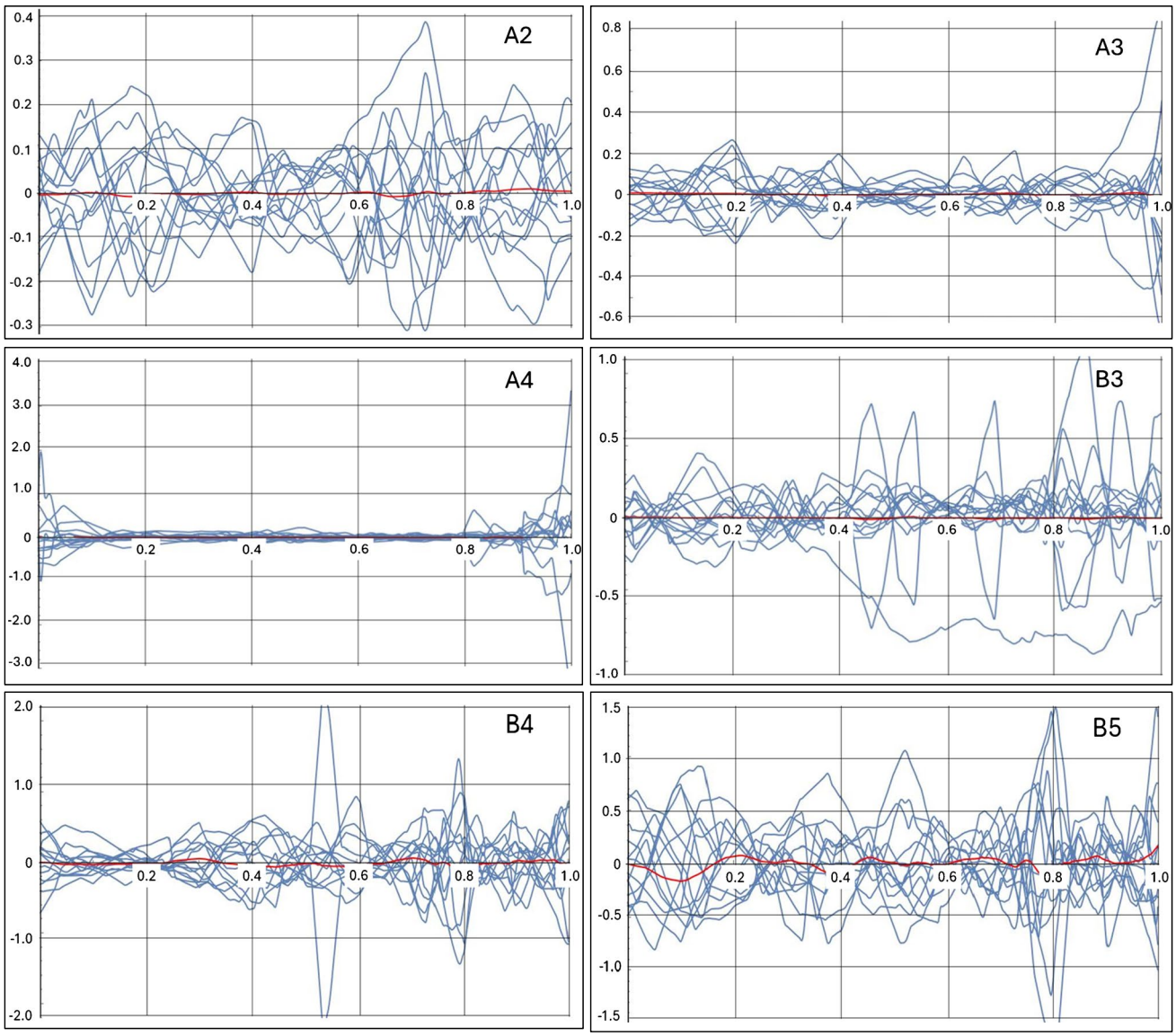

Fig. 4 Representation of the prediction obtained using VEKI and the sample. The prediction of using the VEKI method is shown in red, added to the graphics of Fig. 3 previously described

There are different measurements of error between the curve obtained by prediction and the reality. The commonest ones are the functional root-mean-squared error (E1) (Table 2), functional mean absolute error (E2) (Table 3), and mean absolute error (E3) (Table 4). The following three tables show these three types of error in metres between the prediction using the method VEKI and the real values for 2024 in the six profiles studied. In Tables 2, 3, and 4, the errors are shown for the profiles of maximum slope of cone A (A2, A3, A4) and those of maximum slope of cone B (B3, B4, B5).

Table 5 shows the comparison of errors committed using the methods EK and VEKI for the profiles studied. VEKI is observed to show that the errors defined in almost all cases are smaller (17 from 18), except in E1 (B4) of VEKI. In this way, it is possible to affirm that the variant proposed in this study, that is to say, the VEKI method, represents an improvement to the predictive method of the dynamic of debris cones under study compared with the EK method used in Sanjosé-Blasco et al. (2020). The errors obtained in profiles B3, B4, and B5 of cone B are greater than those obtained in profiles A2, A3, and A4 of cone A. This is due to the fact that debris cone B is made up of stones (at its base) of greater size (up to 1 m), as can be seen in Fig. 2.

Conclusions

Terrestrial laser scanning technology (TLS) has shown a high level of efficiency in accurately tracking short- and medium-term trends in surface movement, as well as yearly surface changes. The deep understanding of sediment transference mechanisms in mountain slope systems is made easier by the use of this method. Data on yearly topographic changes and the movement of sediments from the walls to the cones in a cascade sediment system were obtained

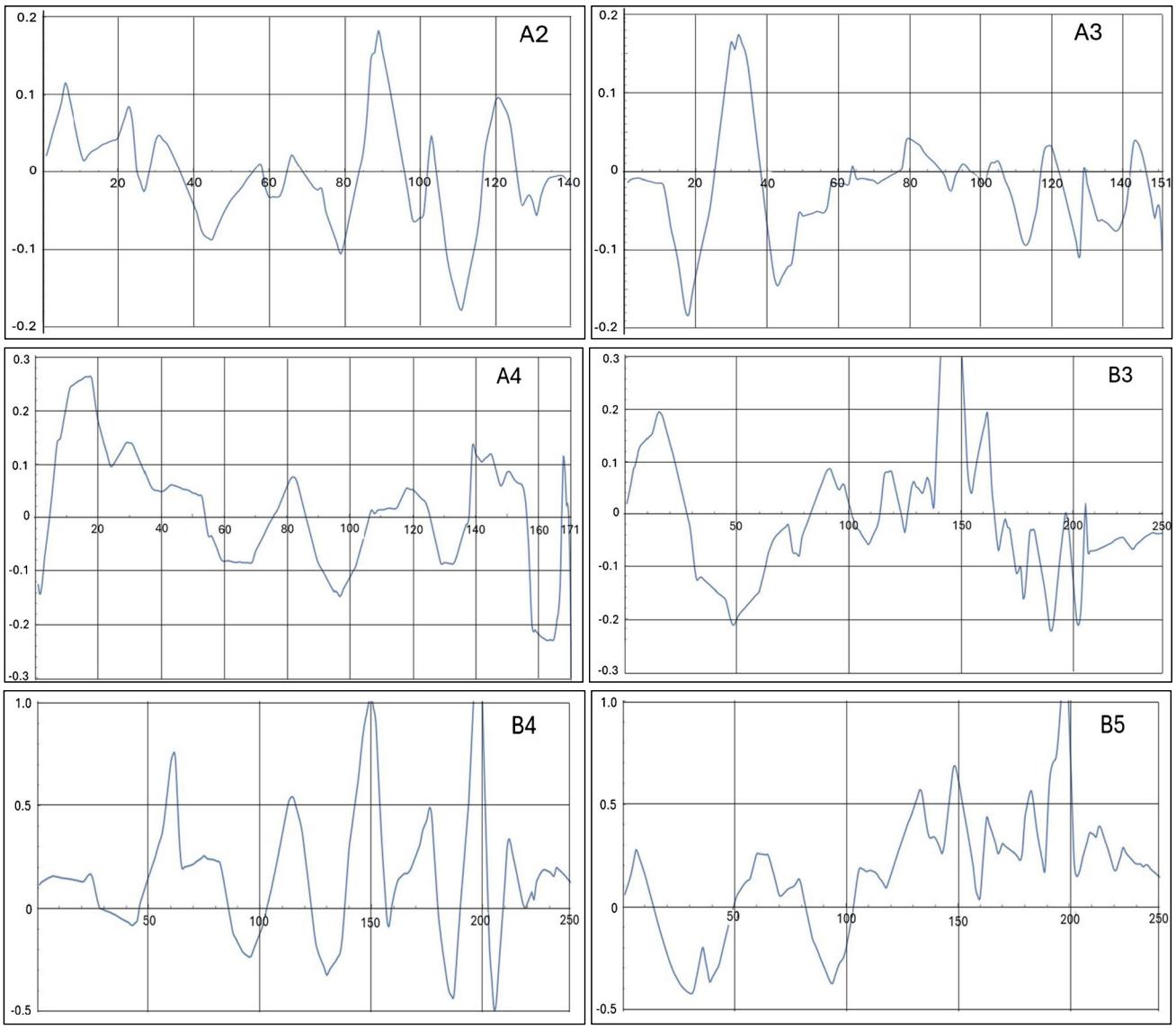

Fig. 5 Differences between the data interpolated predicted by the VEKI method and the real interpolated data in 2024 for each of the six profiles

Table 2 (E1) The mean functional quadratic error obtained with VEKI for each of the six profiles

$A2 = \frac{1}{140}\sqrt{\int_1^{140}(f(t)-g(t))^2 dt} = 0.064936$ m	$A3 = \frac{1}{151}\sqrt{\int_1^{151}(f(t)-g(t))^2 dt} = 0.065963$ m
$A4 = \frac{1}{171}\sqrt{\int_1^{171}(f(t)-g(t))^2 dt} = 0.112422$ m	$B3 = \frac{1}{240}\sqrt{\int_1^{240}(f(t)-g(t))^2 dt} = 0.102151$ m
$B4 = \frac{1}{250}\sqrt{\int_1^{250}(f(t)-g(t))^2 dt} = 0.357781$ m	$B5 = \frac{1}{250}\sqrt{\int_1^{250}(f(t)-g(t))^2 dt} = 0.347853$ m

during independent TLS data collection from two debris cones in the temperate high mountain (Picos de Europa, Spain).

The debris cone shows a changing profile with undulating flow in the distal portion, dominated by slide, flow, and mass wasting. In the middle and upper positions, the solifluction, creeping, and rolling are the dominant processes. The profile is stable, indicating the permanence of the spatial organization of processes over 14 years of geomatic monitoring.

Table 3 (E2) Integral mean of the difference obtained using VEKI in each of the six profiles

$A2 = \frac{1}{140}\sqrt{\int_1^{140}\lvert f(t)-g(t)\rvert dt} = 0.498901$ m	$A3 = \frac{1}{151}\sqrt{\int_1^{151}\lvert f(t)-g(t)\rvert dt} = 0.047269$ m
$A4 = \frac{1}{171}\sqrt{\int_1^{171}\lvert f(t)-g(t)\rvert dt} = 0.088823$ m	$B3 = \frac{1}{240}\sqrt{\int_1^{240}\lvert f(t)-g(t)\rvert dt} = 0.146601$ m
$B4 = \frac{1}{250}\sqrt{\int_1^{250}\lvert f(t)-g(t)\rvert dt} = 0.268516$ m	$B5 = \frac{1}{250}\sqrt{\int_1^{250}\lvert f(t)-g(t)\rvert dt} = 0.285833$ m

Table 4 (E3) Mean discrete error obtained in each of the six profiles using VEKI

$A2 = \frac{1}{140}\sum_1^{140}\lvert \text{Real}_i - \text{Prediction}_i\rvert = 0.050066$ m	$A3 = \frac{1}{151}\sum_1^{151}\lvert \text{Real}_i - \text{Prediction}_i\rvert = 0.047734$ m
$A4 = \frac{1}{171}\sum_1^{171}\lvert \text{Real}_i - \text{Prediction}_i\rvert = 0.092022$ m	$B3 = \frac{1}{240}\sum_1^{240}\lvert \text{Real}_i - \text{Prediction}_i\rvert = 0.102355$ m
$B4 = \frac{1}{250}\sum_1^{250}\lvert \text{Real}_i - \text{Prediction}_i\rvert = 0.270864$ m	$B5 = \frac{1}{250}\sum_1^{250}\lvert \text{Real}_i - \text{Prediction}_i\rvert = 0.288108$ m

Table 5 Errors in metres in the prediction of the curve of 2024 in the 6 profiles using methods EK and VEKI

	EK (A2)	VEKI (A2)		EK (A3)	VEKI (A3)		EK (A4)	VEKI (A4)
E1	0.065352	0.064936	E1	0.069728	0.065962	E1	0.137439	0.112422
E2	0.050037	0.049890	E2	0.051526	0.047269	E2	0.101142	0.088823
E3	0.050181	0.050066	E3	0.052421	0.047734	E3	0.104096	0.092022
	EK (B3)	VEKI (B3)		EK (B4)	VEKI (B4)		EK (B5)	VEKI (B5)
E1	0.105618	0.102151	E1	0.339792	0.357781	E1	0.396373	0.347853
E2	0.148736	0.146601	E2	0.270313	0.268516	E2	0.341565	0.285833
E3	0.105778	0.102355	E3	0.272484	0.270864	E3	0.344410	0.288108

This study's TLS accuracy was ± 2 cm for every measurement site. In the DEMs, scanning the same cone twice on the same day resulted in generation discrepancies of less than 10 cm. Only a few isolated instances showed variances of 15 cm or less, which corresponded to the size of the clasts. Blocks longer than 1 m were found in Cone B's distal region, and the variances between the two DEMs created on the same day were more than 15 cm and nearly 1 m.

In order to forecast the evolution of the debris cones, functional data analysis approaches are used in conjunction with the debris cone study. The yearly data are values that are part of the curves or annual values that define the debris cones, even if they are gathered from a discrete data collection. The analysis and prediction of functional data are two statistical techniques that have emerged in recent years that respect the continuous nature of occurrences of this type.

In Section 3.2, functional data have been applied to represent and analyse the field data necessary for the study of debris cone dynamic. In spite of the fact that the annual data collected is a discrete set, it can be seen that the points on the curves trace these cones. In recent years, statistical techniques have been developed in the name of functional data analysis, which respect the continuous nature of this kind of natural phenomenon.

The present study used some of these techniques to predict the displacement curves of 2024 by fitting the model to the sample of curves of such movement in previous years. Moreover, while the work developed, the real values corresponding to the curves of 2024 were measured. Thanks to these three different measurements of error in the prediction of the curve and the real curve have been possible, and very good results have been obtained using VEKI, a novel variant proposed by the authors of this study that improved prediction in 17 of the 18 predictions made compared with the EK method, which was used in Sanjosé-Blasco et al. (2020).

Finally, it is worth mentioning that the measurement of Eulerian displacements along with the predictive methods applied in this paper can lead to a realistic prediction of the deformation process of the debris cones, which is essentially governed by Lagrangian displacements.

Funding

Open Access funding provided thanks to the CRUE-CSIC agreement with Springer Nature. This publication received funding granted by the Consejería de Educación, Ciencia y Formación Profesional de la Junta de Extremadura, and by the European Regional Development Fund of the European Union through the reference grant GR24156.

Declarations

Conflict of interest The authors declare no competing interests.

References

Ballantyne CK (2002) Paraglacial geomorphology. Quat Sci Rev 21:1935–2017

Becht M, Haas F, Heckmann T, Wichmann V (2005) Investigating sediment cascades using field measurements and spatial modelling. Proceed Sediment Budget Int Assn Hydrol Sci Foz do Iguaçu, Brazil 291:206–2013

Bithell M, Richards KS, Bithell EG (2014) Simulation of scree-slope dynamics: investigating the distribution of debris avalanche events in an idealized two-dimensional model. Earth Surf Processes Landf 39:1601–1610

Bosq D (2000) Linear processes in function spaces: theory and applications; Springer Science & Business Media: New York, USA, 149, 1461211549

Carson MA (1977) Angles of repose, angles of shearing resistance and angles of talus slopes. Earth Surf Processes 2:363–380

de Sanjosé-Blasco JJ, López M, Serrano E, Alonso E (2020) Modelling and terrestrial laser scanning methodology (2009–2018) on debris cones in temperate high mountains. Remote Sens 12(4):632

Didericksen D, Kokoszka P, Zhang X (2011) Empirical properties of forecasts with the functional autoregressive model. Comput Stat 27:285–298

Farias P (1982) La estructura del sector central de los Picos de Europa. Trab Geol 12:63–73

Gardner JS (1983) Accretion rates on some debris slopes in the Mt. Rae area, Canadian Rocky Mountains. Earth Surf Processes Landf 8:347–355

González-Trueba JJ, Serrano E (2010) La nieve en los Picos de Europa: Implicaciones geomorfológicas y ambientales. Cuad Investig Geográfica Geogr Res Lett 36:61–84

González-Trueba JJ, Gómez-Lende M, González-García M, Serrano E (2012) Mapa Geomorfológico de la Orla Sur del Parque Nacional de los Picos de Europa. OAPN-Ministerio de Medio Ambiente: Madrid, Spain, ISBN 848014775X

González-Trueba JJ (2007) Geomorfología del Macizo Central del Parque Nacional de Picos de Europa [con mapa geomorfológico del Macizo Central de Picos de Europa E 1: 25.000]; OAPN-Ministerio de Medio Ambiente: Madrid, Spain, ISBN 8480147008

Hétu B (1990) Évolution récente d'un talus d'éboulis en milieu forestier, Gaspésie. Québec Géographie Phys Quat 44:199–215

Hétu B, Vandelac P (1989) La dynamique des éboulis schisteux au cours de l'hiver, Gaspésie septentrionale. Québec Géographie Phys Quat 43:389–406

Kotarba A, Klapa M, Midriak R, Petras J, Sroka J (1979) Field experiments on high mountain slopes of the Tatra Mts. Stud Geomorphol Carpato-Balcanica Krakow 13:131–148

Luckman B (1988) Debris accumulation patterns on talus slopes in Surprise Valley. Alberta Géographie Phys Quat 42:247–278

Mas A, Pumo B (2009) Linear processes for functional data. arXiv. arXiv:0901.2503

Otto J, Schrott L, Jaboyedoff M, Dikau R (2009) Quantifying sediment storage in a high alpine valley (Turtmanntal, Switzerland). Earth Surf. Processes Landf. J Br Geomorphol Res Group 34:1726–1742

Papa MN, Sarno L, Ciervo F, Barba S, Fiorillo F, Limongiello M (2016) Field surveys and numerical modeling of pumiceous debris flows in Amalfi Coast (Italy). Int J Eros Control Eng 9:179–187

Pisabarro A, Pellitero R, Serrano E, Gómez-Lende M, González-Trueba JJ (2017) Ground temperatures, landforms and processes in an Atlantic mountain. Cantabrian Mountains (Northern Spain). CATENA 149:623–636

Ramsay JO, Silverman BW (2005) Functional data analysis. Springer, New York, USA

Reynard E, Lambiel C, Lane SN (2012) Climate change and integrated analysis of mountain geomorphological systems. Geogr Helv 67:5–14

Sass O, Krautblatter M (2007) Debris flow-dominated and rockfall-dominated talus slopes: genetic models derived from GPR measurements. Geomorphology 86:176–192

Schrott L, Adams T (2002) Quantifying sediment storage and Holocene denudation in an Alpine basin, Dolomites. Italy Zeitschrift Für Geomorphol Suppl 128:129–145

Selby MJ (1982) Hillslope materials and processes. Oxford University Press, Oxford, UK, p 264

Serrano E, González-Trueba JJ (2004) Morfodinámica periglaciar en el grupo Peña Vieja (Macizo Central de los Picos de Europa-Cantabria). Cuaternario y Geomorfología 18(3–4):73–88

Serrano E, González-Trueba JJ, Sanjosé JJ, Del Rio LM (2011) Ice patch origin, evolution and dynamics in a temperate high mountain environment: The Jou Negro, Picos de Europa (NW Spain). Geogr Ann Ser A Phys Geogr 93:57–70

Serrano E, González-Trueba JJ, González-García M (2012) Mountain glaciation and paleoclimate reconstruction in the Picos de Europa (Iberian Peninsula, SW Europe). Quatern Res 78:303–314

Serrano E, Sanjosé JJ, Gómez-Gutiérrez Á, Gómez-Lende M (2019) Surface movement and cascade processes on debris cones in temperate high mountain (Picos de Europa, northern Spain). Sci Total Environ 649:1323–1337

Serrano E, González-Trueba JJ (2010) La dinámica geomorfológica actual de alta montaña y montaña media. In Geomorfología del Macizo Occidental del Parque Nacional de Picos de Europa; OAPN-Ministerio de Medio Ambiente: Madrid, Spain, 79–108

José Juan de Sanjosé-Blasco (✉)
Departamento de Expresión Gráfica, Instituto de Investigación INTERRA, Grupo de Investigación NEXUS, Universidad de Extremadura, Avenida de la Universidad s/n, 10003 Cáceres, Spain
Email: jjblasco@unex.es

Mariló López
Department of Mathematics and Computer Science Applied to Civil Engineering, Polytechnic University of Madrid, Calle del Profesor Aranguren 3, 28040 Madrid, Spain

Enrique Serrano
Department of Geography, PANGEA Research Group: Natural Heritage and Applied Geography, University of Valladolid, Plaza del Campus s/n, 47011 Valladolid, Spain

Estrella Alonso · Javier Rodrigo
Department of Applied Mathematics, Technical School of Engineering, Comillas Pontifical University, Calle de Alberto Aguilera 25, 28015 Madrid, Spain